2016-01-0609

Numerical Investigation of Spark Ignition Events in Lean and Dilute Methane/Air Mixtures using a Detailed Energy Deposition Model

Author, co-author (Do NOT enter this information. It will be pulled from participant tab in MyTechZone)

Affiliation (Do NOT enter this information. It will be pulled from participant tab in MyTechZone)

Abstract

It is beneficial but challenging to operate spark-ignition engines under highly lean and dilute conditions. The unstable ignition behavior can result in downgraded combustion performance in engine cylinders. Numerical approach is serving as a promising tool to identify the ignition requirements by providing insight into the complex physical/chemical phenomena. An effort to simulate the early stage of flame kernel initiation in lean and dilute fuel/air mixture has been made and discussed in this paper. The simulations are set to validate against laboratory results of spark ignition behavior in a constant volume combustion vessel. In order to present a practical as well as comprehensive ignition model, the simulations are performed by taking into consideration the discharge circuit analysis, the detailed reaction mechanism, and local heat transfer between the flame kernel and spark plug. The energy profile and the energy source geometry are investigated in detail to represent the physics of electrical discharge. It was observed in the experiments that a sufficiently high ambient pressure is necessary for a successful ignition event in the lean and dilute mixture when the spark plug gap size and primary energy input are held constant. By adopting realistic energy levels, this detailed energy deposition model showed the capability to reasonably present such ignition behavior transition. The unique combination of energy deposition profile and geometry reveals the complexity of electrical discharge during the spark ignition event. The response of the combustible gas to the energy deposition showed dependency on the volumetric energy density, energy source's surface area, temperature gradient at the energy source boundary, as well as the heat transfer condition local to the flame kernel.

Introduction

Fuel-lean operation in spark ignition engines holds the potential to improve thermal efficiency. On one hand, the maximum combustion temperature is reduced due to excess air, thus reducing the total heat loss to the engine block; on the other hand, fuel-lean combustion may serve as an alternative to throttled intake under part loads, which helps to avoid pumping loss. Despite the appealing benefits, the major challenge for such combustion strategy is the increased instability when dilution is present. It is believed that at least three key factors, i.e. the ignition source, the turbulent flow, and the mixture preparation process, are impacting the lean burn behavior.

The ignition source, usually the spark discharge, is believed to affect the ignition behavior by means of the total deposited energy and the manner this energy is released. Multiple attempts [1–5] to manipulate the spark energy profile have shown benefits under specific engine or engine-like conditions. Diverse method descriptions ranging from increasing discharge duration to increasing number of discharges are claimed to be beneficial for successful ignition of lean and dilute fuel-air mixtures. In addition, the existence of turbulent flow in the vicinity of ignition onset is believed to play a key role. The premixed flame front becomes more sensitive to stretch and curvature under fuel-lean conditions, which could lead to propagation failure given that the flow field is unfavorable [6]. Lastly, mixture stratification has been considered a promising strategy to extend the lean operation limit, while it could be quite challenging to deal with the complex stratification controls during transients [7].

Multi-dimensional simulation serves as a powerful tool to investigate the underlying physics of complex phenomena like the ignition process. Efforts to model combustion initiation by electrical discharge date back to 1980's [8]. Spark ignition models have developed over decades by integrating thermodynamics, fluid mechanics, chemical reactions, as well as plasma physics [9–12]. Application of spark ignition models to three-dimensional engine simulations were realized by introducing sub-grid Lagrangian models. Well-developed models such as the DPIK, AKTIM, and SparkCIMM have shown success in a variety of engine applications. More recently, with the increasing computational power of high performance computers, it has become realistic to adopt finer computational meshes to resolve the onset of spark ignition. Such ignition modeling in the pure Eulerian domain appears to be more intuitive, as the sole input reduces to an energy source term deposited into the fluid solver's energy equations. Several recent numerical studies have shown the capability of the Energy Deposition Model in engine combustion simulations [13–15].

Despite the simplicity in setting up the Energy Deposition Model, it was observed that ambiguity arises when several key parameters get assigned. The common practices usually adopt the total deposited energy from spark coil ratings or measurements, while the geometry and temporal profile of the spark energy release are usually chosen relatively arbitrarily given that the flame can be initiated. Such a strategy may not show significant impact on normal combustion cycles since the macroscopic combustion behavior will be dominated by the flame model rather than the ignition model. However, when it comes to an incomplete combustion cycle, the unrealistic inputs to

the ignition model may lead to misinterpretation of the effects of turbulent flow.

In this study, efforts are made to investigate the impact of ignition source on ignition behavior by isolating the flow effect. Inputs to the Energy Deposition Model are studied in detail to reflect more physical characteristics of the process. After some analysis on the appropriate methods to compare optical experimental data and simulation results, the performance of this detailed Energy Deposition Model is assessed, followed by discussions on effects of energy source size, geometry, and heat transfer to electrodes.

Experimental Observations

Numerous experimental observations of spark ignited flame kernels have been performed over decades (e.g. [3,6,16]). The current study starts with a fresh dataset due to the following reasons. First, quiescent flame kernel development is usually studied using needle-shaped electrodes, while in this study it will be more beneficial to adopt an engine spark plug and take into consideration the heat transfer from the flame kernel to the electrodes. Second, detailed measurement of the electric signals are available with this new dataset, allowing for more precise energy calculations. Lastly, results of both successful ignition and quenched flame kernels are readily available for validation.

The experimental study was conducted in a constant-volume combustion vessel with extended optical access. Detailed features of the combustion vessel can be found in [4]. As shown in Figure 1, a modified Z-type schlieren setup was used for visualizing the flame kernel. A Photron FASTCAM SA1.1 high-speed camera was used to capture the ignition process at 25,000 frames per second.

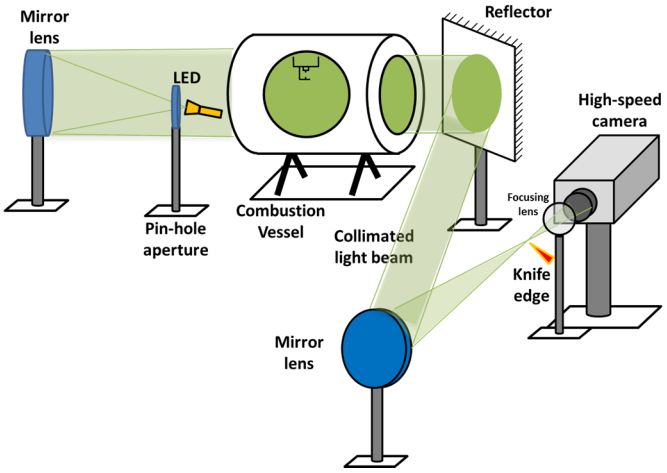

Figure 1. Schematic of optical setup for visualizing spark ignited flame kernel development.

A spark plug with double fine electrodes was mounted through the top surface of the cubical combustion vessel. The ignition system used a typical vehicle coil connected to the spark plug using a high-tension wire. Input to the coil was fixed at 15V primary voltage over 700μs dwell time, and the peak primary current attains 2A. Figure 2 shows a schematic of the secondary circuit and the electric signal sensing locations. As can be seen, the coil, the voltage probe, the spark plug, and the contact connection between the high-tension wire and the spark plug are all contributing to the secondary circuit capacitance. Electric signals are collected using a high-voltage probe (Tektronix P6015A) for secondary voltage and a voltage divider for secondary current. Both signals are recorded with an oscilloscope at 500 kHz. Secondary voltage was measured at the input to the high-tension wire, and the secondary current is sensed at the low side of the secondary circuit, in order to collect all currents from the distributed secondary capacitances.

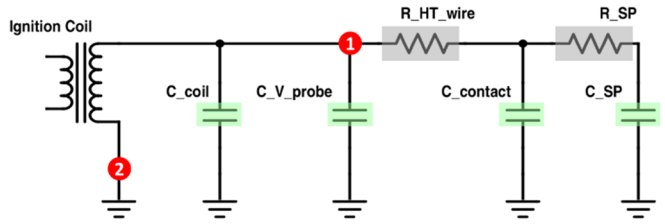

Figure 2. Schematic of secondary circuit of ignition system. Sensing point 1 is for voltage measurement and point 2 is for current measurement.

The combustible mixtures used in the tests are prepared using a process control system. Each gas component is filled sequentially into a mixing tank following the partial pressure law, and the filling order and mole fractions of each component is shown in Table 1. This mixture is corresponding to an equivalence of 0.6 and carbon dioxide is added as dilution. The filling process is monitored by pressure transducers to ensure accuracy and consistency of the mixture. A brief description of the test procedure is described below. Prior to the tests, the combustion vessel is preheated to 423 K and kept at constant temperature with feedback controlled heaters. During the tests, the vessel is first purged twice with the combustible mixture to above 4 bar pressure to ensure correct mixture composition. At the third filling, the combustion vessel is filled to the desired test pressure and all valves are sealed to create a closed system. After a residence time of about 1 minute, the spark is triggered. The camera is triggered 1 ms prior to the spark event and records up to 5 seconds of high speed frames. The vessel is purged with nitrogen at the end of each test run.

Table 1. Combustible mixture components and their filling order during preparation.

Filling Order	Gas Component	Mole Fraction
1	CH_4	5.5%
2	CO_2	0.6%
3	N_2	75.4%
4	O_2	18.5%

Spark plug gap size and the initial pressure prior to spark are the two independent variables during the tests and the ignition behavior is recorded. For premixed combustion, a successful ignition will lead to propagation of the flame front throughout the mixture domain. However, two kinds of ignition failure may occur. The first type corresponds to the case in which the electrical discharge is formed and a flame kernel is generated, but the flame front quenches before it consumes all the combustible mixture. We may name such ignition failure as “fail to propagate”. In the second type failure, the electrical discharge is not generated, usually because the electrical energy stored in the coil is not sufficient to breakdown the gases. Thus the second type could be called “fail to spark”. While the second type failure could be resolved by adopting a higher energy coil, the first type failure is more closely related to the complex combustion process, and will be the type of ignition failure to discuss in this

paper. All the tests are operated in a regime where electrical spark can be formed.

Experimental results are summarized in Figure 3. A total number of 11 combinations of spark plug gap sizes and initial pressures are tested under quiescent conditions with the same mixture and electrical input to the ignition coil. Each combination is repeated for 3 to 4 runs as labeled beside each test point in Figure 3. It can be seen from this summary that for a given spark plug gap size, a transition from successful ignition to failure will occur as the initial mixture pressure decreases. Such transition pressure value lies between 1.38 bar (20 psi) and 2.76 bar (40 psi) for gaps of 1 mm or larger, while its level and uncertainty both increase for smaller gaps. Numerical investigations are carried out to understand this transition in detail. The experimental data obtained for 1.2 mm gap have shown clear transition when pressure drops from 2.76 bar to 1.38 bar. Furthermore, the same behavior are also observed for slightly larger (1.4 mm) and smaller (1.0 mm) gap sizes, which potentially increases the confidence level of the 1.2 mm gap data, thus the results for 1.2 mm gap are adopted as major dataset to validate against.

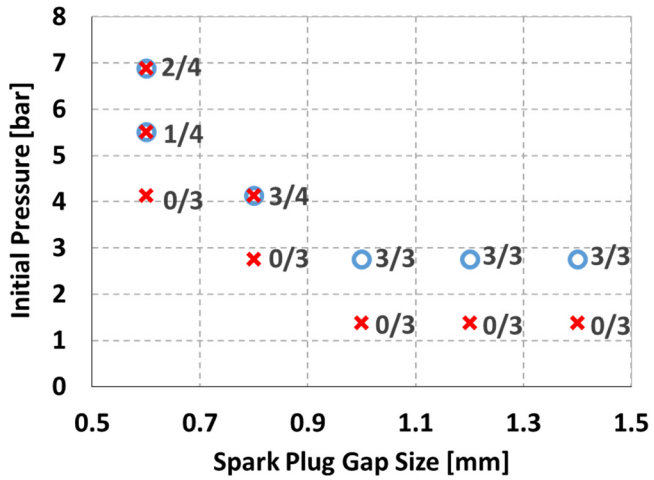

Figure 3. Summary of ignition results at variable gap sizes and initial pressures. "○" symbol represents ignition success and "×" for failure. The fraction adjacent to the symbols indicates the number of ignition successes over the total number of test runs.

Energy Deposition Model Details

General Model Description

A small section near the spark plug at the top surface of the combustion vessel is extracted as the domain of this simulation. As seen in Figure 4, the spark plug electrodes, spark plug adapter, and a square portion of the top combustion vessel surface are flagged in pink, and serve as the top boundary of the fluid region. The remaining fluid boundaries are defined as open boundary as the extracted section is much smaller than the full vessel volume of 1.1L. In order to investigate the heat transfer processes during the ignition event, a solid portion is added behind the top fluid boundary and sealed by an extra solid boundary (labeled orange in Figure 4). The space between the orange surface and the pink surface is filled with stainless steel, which is the material of the combustion vessel. According to the experimental conditions, the initial temperature for both fluid and solid region are defined at 423K, and the initial gas pressure is set to 2.76 bar and 1.38 bar, respectively for successful ignition and failure cases.

The numerical simulations are performed with CONVERGE, a general purpose computational fluid dynamics code that calculates incompressible or compressible, chemically-reacting fluid flows in complex three-dimensional geometries. CONVERGE's automated mesh generation based on modified cut-cell Cartesian method [17] helps to simplify the modeling process. Simple orthogonal Eulerian grids with embedded mesh refinements are used in this study. The base mesh size used is 1 mm and multiple layers of mesh embedding up to level 4 are used to achieve a grid size of 62.5 μm near the spark plug without abrupt cell scaling. One-dimensional flame simulations with the same chemistry are performed under the same initial conditions. The lean and dilute fuel/air mixture under relatively low pressures as used in this study usually yields thick flame. The laminar flame thicknesses of the mixture are 0.55 mm and 0.76 mm respectively for 2.76 bar and 1.38 bar initial pressures, for which the 62.5 μm mesh is sufficient to resolve the flame front structure.

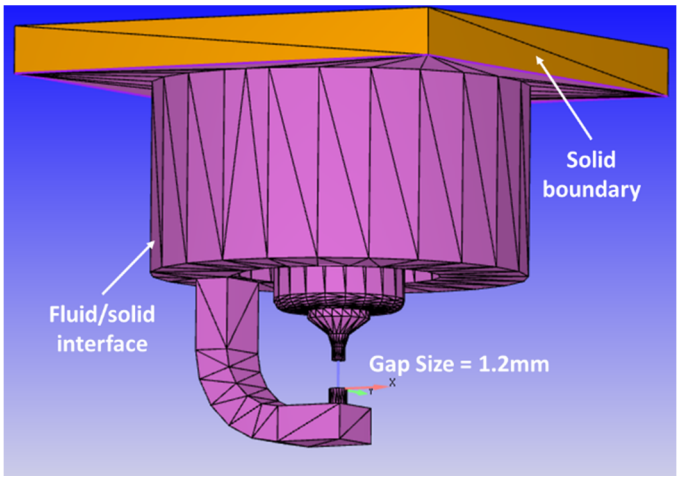

Figure 4. Geometry and boundary assignment of the simulation.

The combustion is simulated through detailed chemistry with reaction rates defined in Arrhenius-type constants. The detailed chemistry intends to more accurately simulate combustion with multiple chemicals and reactions, and is thus essential to the Energy Deposition Model. As the major fuel in the mixture is methane, the GRI-Mech 3.0 [18] was adopted for combustion modeling. Turbulence is resolved by the RNG k-ε RANS model.

Modeling of heat transfer between fluid and solid is achieved by activating the super-cycle modeling in CONVERGE [17]. With well-defined specific heat properties for both the solid and fluid, energy equilibrium calculations are carried out near the phase interface, and the equilibrium temperature is assigned to new boundary conditions for later calculation. In addition, since the time constant for thermal equilibrium is usually larger in solid than in the gases, the time interval for heat transfer calculations can be multiples of the fluid solver to be more time efficient.

Ignition Circuit Analysis

The key input to the Energy Deposition Model is the energy source term, for which the geometry and the temporal power profile need to

be specified. A detailed ignition circuit analysis is hereby performed to obtain realistic numbers from the experiments.

An established theory is readily available that describes the spark discharge process qualitatively as three distinct phases, i.e. the breakdown, arc, and glow discharges [19]. From a microscopic point of view, the theory recognizes the differences in terms of electron sources in order to characterize the discharge modes. During the breakdown phase, the electrons come from the cosmic emission and the avalanches generated by these seed electrons colliding with other neutral particles. Such discharge is quick and intense due to the large amount of participating electrons. Electrons diminish abruptly at the end of breakdown phase as they reach the anode and other sources of electrons are needed to sustain the current. Two mechanisms are able to supply the electrons: thermionic emission from the hot cathode surface, and bombardment of the relatively heavy positive ions on the cathode surface. The arc discharge is associated with the hot cathode surfaces and comes earlier and more intense than the glow phase. The discharge ceases due to insufficient energy in the circuit to maintain the electric field.

Unfortunately, a quantitative description of the electrical discharge is not quite applicable yet. On one hand, although Paschen's Law [20] is available to state the dependency of the breakdown voltage on electrode gap size and the local gas pressure, there are other parameters of uncertainty involving the gas condition and electrode material, making it difficult to predict the breakdown voltage. On the other hand, the correlation between the current/voltage waveforms and their microscopic behavior is still vague. With these knowledge barriers, it would be challenging to derive the ignition energy profile from the theoretical analysis.

Thus it would be more realistic to calculate the energy profile from experimental measurements. Calorimetry for spark energy estimation has been proposed for decades [21,22]. The electrical energy is discharged into a limited volume of insulated and closed gas system, and the gas pressure increase is measured to obtain the estimation of discharged energy. However, due to the relatively demanding test conditions and the fact that the used gas is usually inert, calorimetry is not used in this set of tests.

The secondary current and voltage waveforms are obtained instead to provide a direct estimation of the energy inputs, and a detailed loss analysis over the circuit is performed. The measured secondary current and voltage are filtered to remove high-frequency noise and presented in Figure 5. The zero timing is aligned with the peak secondary voltage, which is believed to correspond to the breakdown voltage. As can be seen in the waveforms, the secondary signals begin to increase before the breakdown occurs. This duration is also referred as the pre-breakdown phase, during which the induction from the primary coil is charging the secondary capacities. The distributed secondary capacities (Figure 2) act as reservoirs that temporarily store the inducted energy from the primary side before the conductive plasma channel is formed. At the onset of discharge, the voltage experiences an abrupt drop, which is accompanied by the release of the capacity-stored energy, resulting in the intense breakdown discharge within nanoseconds. The nanosecond breakdown phase is not likely to be recorded by the waveform measurement, and some conversions are needed to calculate the breakdown energy. For this study, the integration of electric power during the pre-breakdown phase is treated as the breakdown energy. The breakdown energy is determined using Eq. (1).

$$E_{bd} = \int_{pre-bd} i(t)v(t)dt \quad (1)$$

The product of secondary current and voltage is plotted with respect to time and is shown in Figure 6. The curve indicates the power of electric current in the secondary circuit, and the area under the power curve is the released electrical energy. As discussed, the breakdown energy equals approximately to the stored energy during the pre-breakdown phase, thus the green-shaded area in Figure 6 with timestamps before zero timing can be treated as the breakdown energy. Note that an alternative method for breakdown energy calculation is presented in [22], which is equivalent to the calculation performed above given that the secondary capacitance is assumed constant.

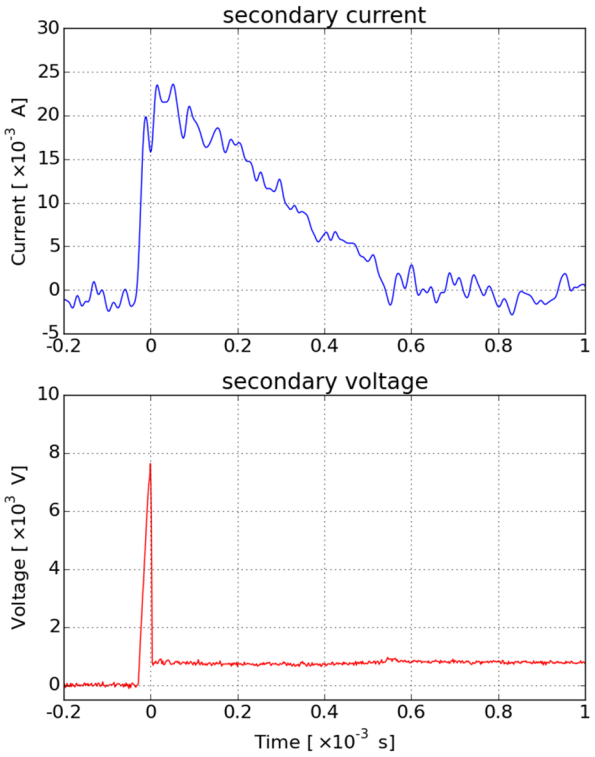

Figure 5. Sample waveforms of secondary current and voltage.

The discharge energy after breakdown can be calculated ordinarily by integrating the electric power over time, since the current and voltage signals do not experience large variations that could cover orders of magnitude as during the breakdown phase. This part of discharge energy is labeled in pink in Figure 6 and denoted as arc/glow energy. Unlike the breakdown energy, the arc/glow energy mostly comes from the coil rather than the capacitance, and is subject to resistance losses in the circuit. The two major electrical resistances in the secondary circuit are the high-tension wire and the spark plug, each contributes about 5000 ohm according to separate measurement, and heat losses over these resistances need to be subtracted from the discharge energy to the gases. As a result, the calculated electrical energy released can be obtained by Eq. (2) below.

$$E_{discharge} = E_{bd} + \int i(t)v(t)dt - \int i(t)^2 R dt \quad (2)$$

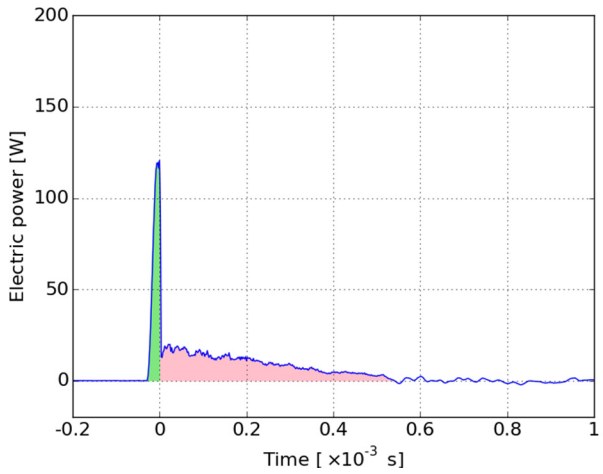

Figure 6. Sample electric power profile.

A recent study [22] has also discussed the energy losses during spark discharge in detail. On a more detailed level, the reference states that the voltage between the electrodes consists of three components, i.e. the anode fall, cathode fall, and the positive column voltage. The electrode falls are caused by the near electrode fields and properties within these falls can be quite different with the majority of the plasma. Empirical equations are used to quantify electrode falls and energy released within the near-electrode layers is considered as the loss to electrodes. Nonetheless, the authors of the present paper have found it difficult to apply the same sets of empirical equations to the gas mixture used in this study. Thus a simplification is made by assuming uniform energy deposition in the plasma channel and letting the conjugate heat transfer models handle the electrode losses.

The resulting energy profiles for 2.76 bar and 1.38 bar are listed in Table 2. The breakdown energy is released in the first microsecond, and the arc/glow energy is released with decaying power to resemble the actual profile. A representative schematic of the energy profile is also listed in Table 2. Higher breakdown energy is released in the high initial pressure case, which agrees with the Paschen's Law trend. In addition, for the lower pressure case, due to less released energy during breakdown, the discharge duration gets extended to dissipate energy from the coil in the arc/glow modes. The dimension of the plasma channel is usually estimated on the order of 100 µm in diameter [19,23–25]. Due to the lack of direct measurement, two levels of channel sizes are tested in the numerical study. The discharge channel is represented by a column of computational cells across the spark plug, and the cross section is square with 62.5 µm and 125 µm side lengths respectively for the two channel sizes.

Table 2. Energy profile details for 2.76 bar and 1.38 bar ignition cases.

	E_bd	**E_arc/glow**	**Duration**	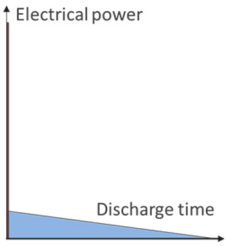
2.76 bar (40 psi)	1.90 mJ	4.20 mJ	550 µs	
1.38 bar (20 psi)	1.70 mJ	4.46 mJ	680 µs	

Results and Discussion

Numerical results of CFD simulations are presented and discussed in this part. A brief overview of the general pattern of the simulation results is first performed to narrow down the parameters to inspect, and then the effect of energy source terms' geometry, size, heat transfer effect, and mesh size effect are discussed.

Representative Output Variables

The successfulness of the ignition event can be verified by the temporal history of total heat release rate from the chemical reactions. The failure case ends with a zero heat release rate well before all the fuel is burnt. Under the baseline setup, the minimum computation cell size is 62.5 µm and the ignition source is deposited in one column of such cells across the electrodes that are 1.2 mm apart. With the calculated energy profile, successful ignition is reproduced under 2.76 bar initial pressure, while ignition failure is observed under 1.38 bar initial pressure, indicating the Energy Deposition Model with realistic energy inputs is able to correctly predict the ignition behavior under these tested conditions. Several insights of the transient ignition process are presented in the following.

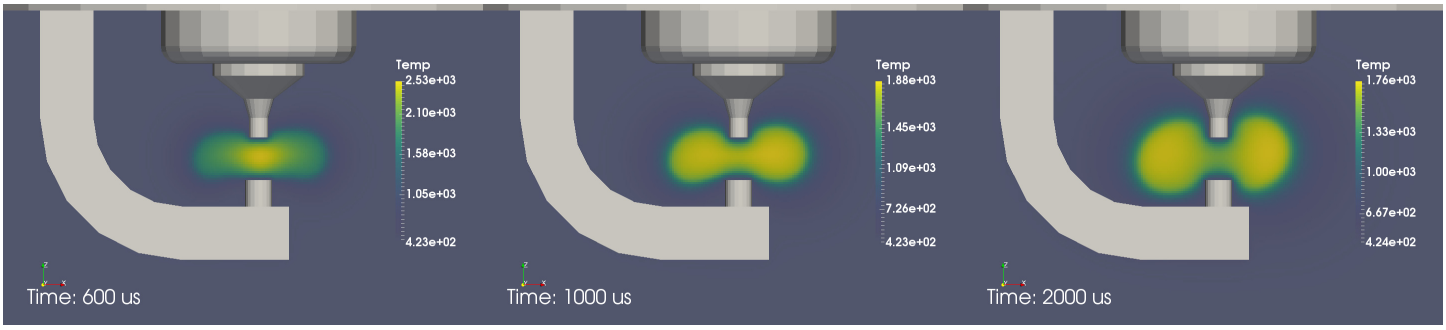

Figure 7. Snapshots of temperature distribution of the flame kernel in a center slice of the simulation domain. The showing case is corresponding to 2.76 bar initial pressure. Different color map scales are used for better representation of the distribution at each time step.

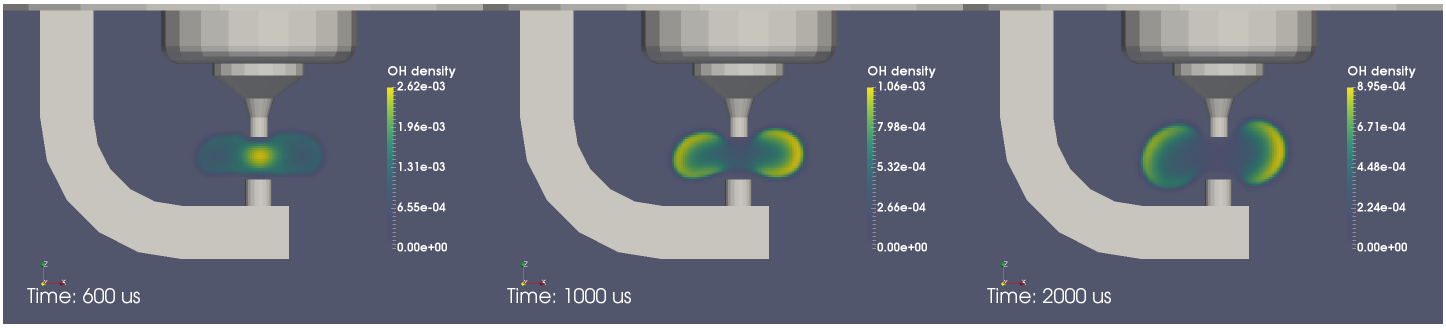

Figure 8. Snapshots of OH radical density distribution of the flame kernel in a center slice of the simulation domain. The showing case is corresponding to 2.76 bar initial pressure. Different color map scales are used for better representation of the distribution at each time step.

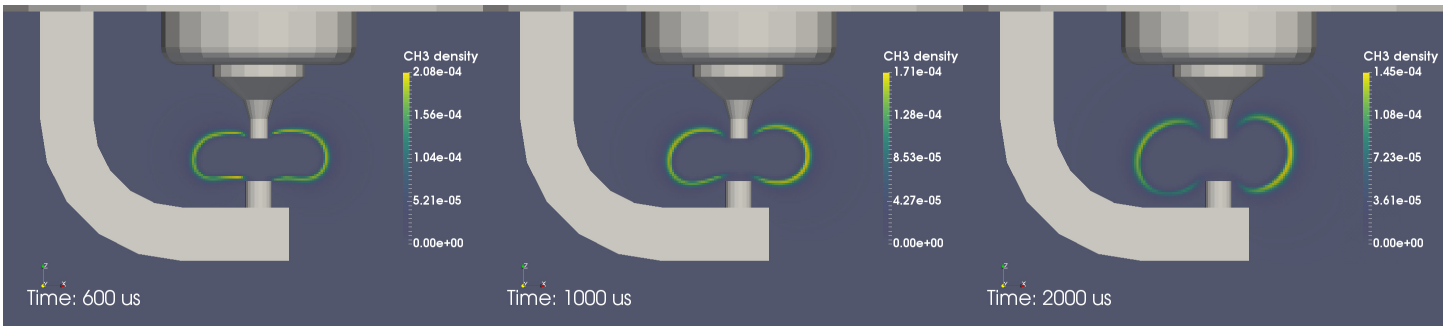

Figure 9. Snapshots of CH_3 radical density distribution of the flame kernel in a center slice of the simulation domain. The showing case is corresponding to 2.76 bar initial pressure. Different color map scales are used for better representation of the distribution at each time step.

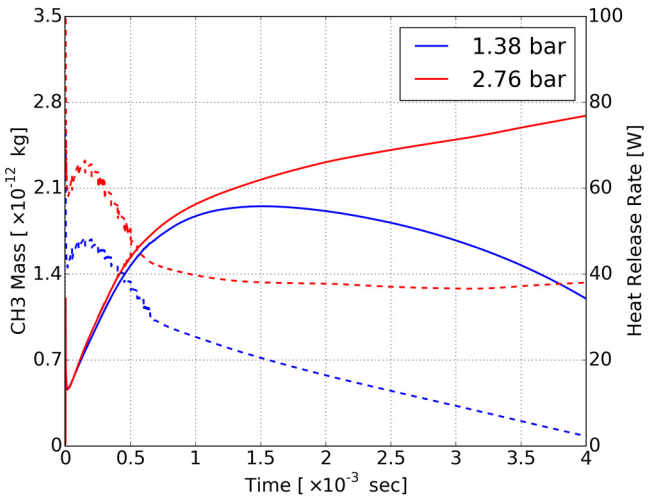

Figure 10. Overall ignition simulation behavior for 2.76 bar and 1.38 bar under baseline setup. Solid lines represent total CH_3 mass, and dashed lines represent total heat release rate.

Temperature is intuitively a representative output variable of the flame kernel. Snapshots of temperature distributions have been extracted from a center slice of the simulation domain. Figure 7 presents a series of such snapshots from the 2.76 bar initial pressure case. Right after the end of electrical discharge at 600 µs, the high temperature region extends mainly horizontally from the spark plug gap with the highest temperatures concentrated within the gap. At 1 ms, without the support of external energy deposition, the high temperature region grows relatively slowly on its own. The kernel expands in a larger step in the vertical direction than in horizontal, and the expansion mainly happens away from the electrodes. The temperature distribution gets more even within the kernel region, which resembles a theoretical premixed flame front with hot burnt product and cold unburnt mixture on both side of the flame. At an even later timing of 2 ms, the self-sustaining kernel keeps expanding and the peak temperature is getting closer to the adiabatic flame temperature (approximately 1700 K). The high temperature region still presents relatively uniform temperature distribution except that the regions near the spark plug gap is colder, which could be the effect of heat transfer to the electrodes.

In addition to temperature, the detailed-chemistry-enabled combustion model also make it possible to access certain species as combustion indicators. OH radicals are of interest for experimentalists and their snapshots of center slice from the 2.76 bar case are shown in Figure 8. It can be seen that the shape of the OH distribution agrees quite well with that of the temperature at each time step, while the magnitudes are uneven. In the 600 µs snapshot, the peak OH density coincides with the peak temperature in between the electrodes, which is implying the OH is more likely to be formed at high temperature zones. Thus it is also reasonable to see high OH concentration at the boundary of the kernel which is closer to the flame front at later time steps when the kernel becomes self-sustained.

Even though the temperature and OH density distributions are comprehensive, they show relatively complex patterns on a 2D slice, and could become more difficult to describe in a 3D fashion. Alternatively, the authors would like to introduce another representative species that could be characteristic to the premixed flame front. As shown in Figure 9, the CH_3 density distributions present quite different features than temperature and OH. Unlike the

other two output variables, CH_3 occupies a concentrated region in the spatial domain, and more importantly, these thin lines appear to lie around the edge of the hot kernel, making it a good representative of the flame kernel. Such feature of the CH_3 distribution is revealing an important fact that CH_3 is a quick and absolute intermediate during combustion as hydrocarbons needs to first disassociate to CH_3 and then further break up to get completely burnt. Tracing the level and presence of CH_3 will lead to a quick overview of the flame kernel's state in terms of size and successfulness.

As discussed above, the overall ignition behavior of a simulation case will be assessed by plotting its temporal profile of total CH_3 mass in the simulation domain and its total heat release rate. The overall simulation behavior is presented in Figure 10 for successful and failed ignition under different initial pressures. The heat release rate is subject to an abrupt increase at the beginning of the energy deposition due to the extremely high power of the breakdown phase, and the subsequent energy deposition causes the heat release rate to first increase and then decrease for both cases. The separation of ignition behavior can be directly related to the difference in energy source terms. The high initial pressure case is also associated with higher energy deposition power during the breakdown phase and at the beginning of the arc/glow phase. The deposited energy essentially raises the flame kernel temperature, which promotes reactions and expansion. The reduced external input at low initial pressure leads to propagation failure due to insufficient combustion heat. Heat losses exceed the reaction released heat and the kernel temperature eventually becomes too low to sustain the reaction.

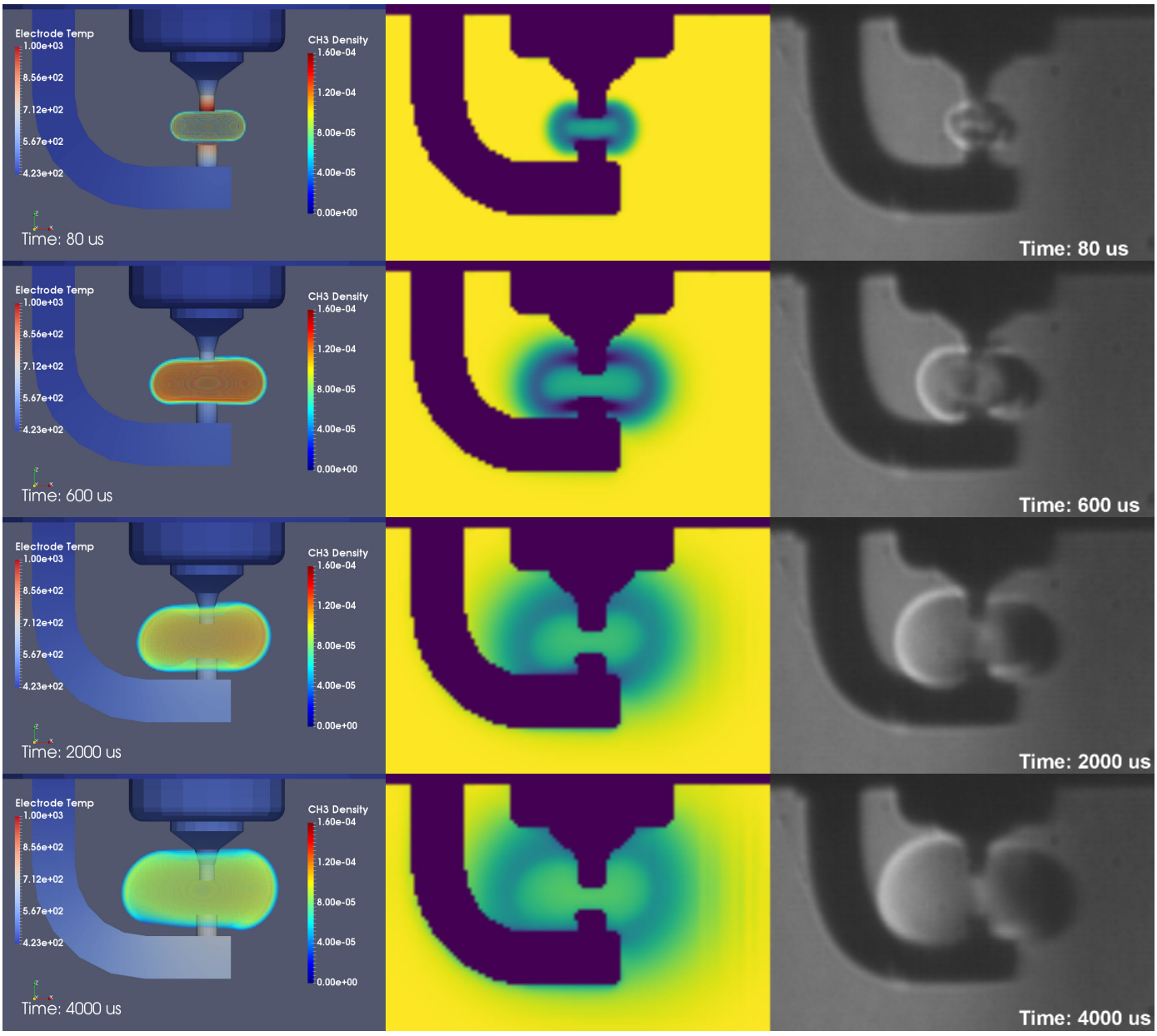

Figure 11. Temporal series of volume-rendered CH_3 distribution, numerical pseudo-schlieren realizations, and optical schlieren images. The showing case is corresponding to 2.76 bar initial pressure. Color map scales in the left column are kept identical across the time steps and with those used in Figure 12.

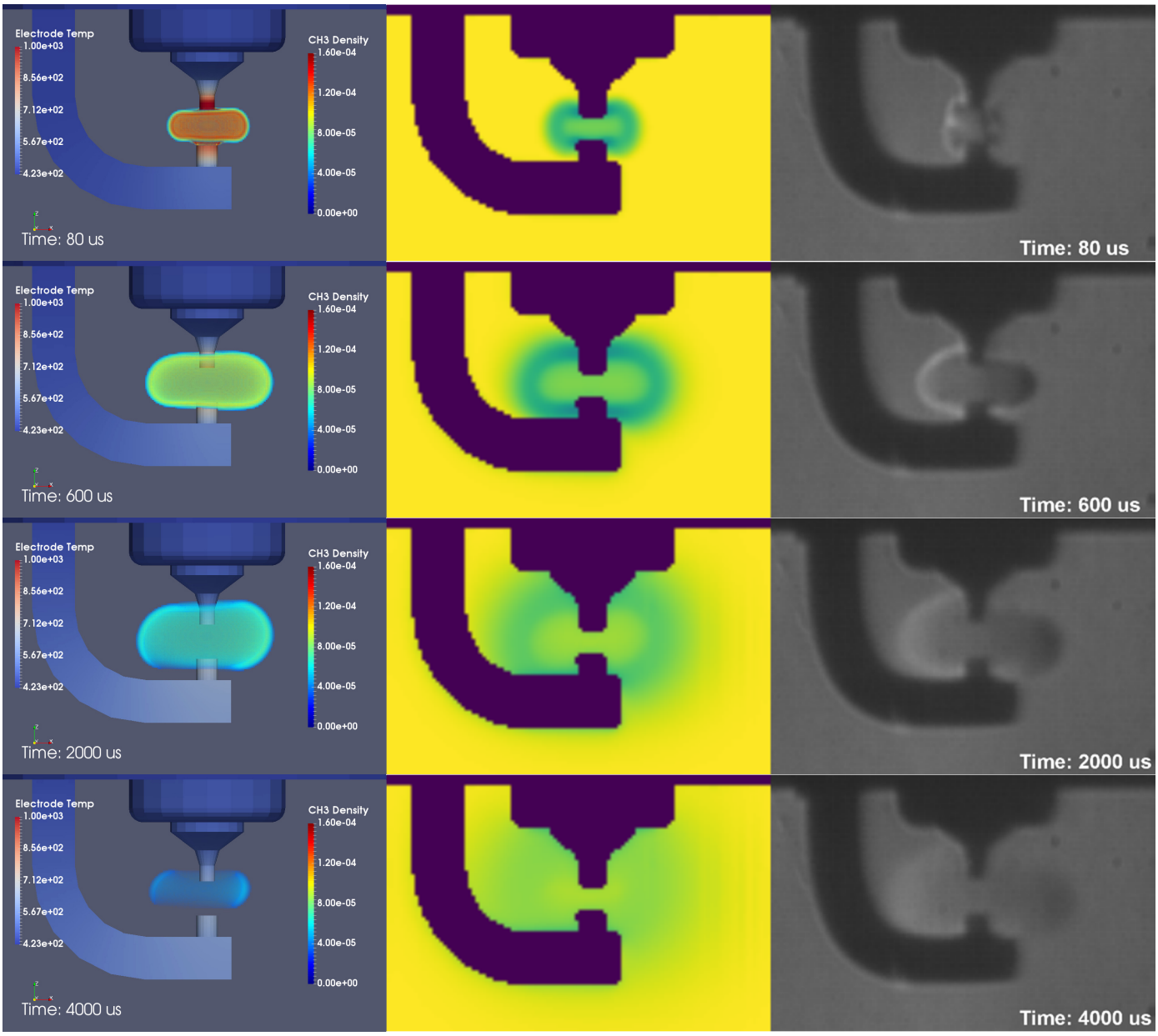

Figure 12. Temporal series of volume-rendered CH_3 distribution, numerical pseudo-schlieren realizations, and optical schlieren images. The showing case is corresponding to 1.38 bar initial pressure. Color map scales in the left column are kept identical across the time steps and with those used in Figure 11.

Flame Kernel Growth

In addition to the fact that the proposed detailed Energy Deposition Model is able to predict the overall ignition behavior, it is more desirable to show that the detailed features of the kernel growth are also properly captured. As illustrated above, CH_3 radicals occupy the outer layer of the flame kernel. However, the direct comparison between volume-rendered CH_3 distributions and the optical schlieren images shows mismatch in terms of kernel shape. Figure 11 and Figure 12 represent two forms of numerical results of kernel growth in comparison with the optical schlieren images for successful and failed ignition cases. In both figures, the left column is for volume-rendered CH_3 distributions, the center column shows pseudo-schlieren realization that will be introduced later in the context, and the right column is the experimental results. As seen in the left column of Figure 11, at early time steps (80 and 600 μs), the simulated kernel matches approximately the horizontal expansion with an obvious underestimation in the vertical direction. And underestimation of the kernel size become more recognizable at later time steps.

Before questioning the simulation parameters, one question to ask is whether the comparison between the CH_3 profile and observed kernel through schlieren is reasonable. A negative answer could become more obvious by inspecting the ignition failure case. As shown in Figure 12, the quenching flame kernel's CH_3 distribution shrinks towards the kernel center where temperature is higher, while the quenching kernel under schlieren is blurring at its boundary from the background. A conversion from 3D numerical simulation results to schlieren-like representations is hereby proposed to achieve more reasonable CFD/experiments comparison. It is well understood that the schlieren imaging is an optical technique that captures the

difference in refractive indexes in a transparent media. The edge of the visualized object is formed due to the gradient of refractive indices along the line of sight. Given the fact that an approximate linear correlation can be obtained between the density and refractive index of a gas, the schlieren images are also believed to represent the density gradient in the spatial domain.

Even though a qualitative description of the schlieren method seems straightforward, it could be challenging to trace the light rays to obtain a numerical schlieren realization [26]. In this paper, a simplified approach is performed. The pseudo-schlieren realization is created by first obtaining the magnitude of the gradient vector of the density field at each spatial location, and then integrating these magnitudes along the line of sight. Results of such pseudo-schlieren methods are presented in the middle columns of Figure 11and Figure 12. It can be seen that with the closer nature of image processing, a better match between the CFD and experimental data can be observed. For the successful ignition case, the pseudo-schlieren method is able to minimize the underestimation in vertical expansion against the CH_3 method. As both the pseudo-schlieren and the CH_3 representation come from the same set of numerical results, it could be inferred that the thickness of the flame front varies spatially. The flame front is thicker close to the relatively cold electrode than facing the open unburnt mixture. On the other hand, the decaying density gradient is also properly reproduced for the ignition failure case. The visual resemblances between the simulated kernel and optical data therefore greatly increased the fidelity of the simulation results.

Lastly, it is also worth mentioning the temporal expansion trend of the spark ignited flame kernels. As shown in the schlieren images in Figure 11, the kernel has shown a faster volumetric expansion in its early development (80 µs to 600 µs) than later stages (2000 µs to 4000 µs). The increased kernel growth rate is due to the thermal expansion induced by the spark. The high power energy source brings the gas temperature to tens of thousands kelvins during the breakdown phase, and the extreme temperature gradient at the spark plug gap produces an outward flow field (shock wave) that essentially increase the effective flame speed. With carefully determined energy source in this model, the effect of faster kernel expansion during the discharge is automatically reproduced.

Effects of Key Parameters

Effect of Energy Source Size

As was discussed in previous sections, the lack of detailed measurement of plasma channel size has resulted in only an estimation of its order of magnitude. In this section, the effect of the energy source size is studied by setting up simulations with thicker lines of energy source. The simulation grids are kept the same (62.5 µm minimum cell size), and the baseline case activates one column of the finest simulation cells, while the thicker line setup activates four columns of cells. Thus the "1 line" source is a column with square cross section of 62.5 µm and the "4 lines" source has a square cross section of 125 µm. The same energy deposition profile is applied, and the overall ignition outcomes are shown in Figure 13 and Figure 14 respectively for 2.76 bar and 1.38 bar initial pressure cases.

The overall model prediction on ignition success/failure does not change by applying the thicker line energy source. However, the CH_3 production and the total heat release rate both experience an increase. In addition, the kernel expansion is also accelerated by the thick line source. Despite the fact that the 4 lines cases have lower spatial energy density than the 1 line cases, the thicker line sources yields slightly faster flame kernel expansion as seen in Figure 15 and that trend is regardless of the ignition outcome. The shifted starting point of the kernel expansion due to the thicker ignition channel would not cover the entire reason for the increased kernel size, as the size difference in the horizontal direction is beyond that of the sources. One other possible cause is the increased contact area of the thicker line source against the unburnt mixture. With the ambiguity of experimental understanding of the ignition channel size, the line source thickness could serve as a tunable parameter in numerical practice for better matching with the optical data. In addition, there is also a possibility that the channel thickness is a variable throughout the ignition event. Testing against such assumptions has been considered future work. The remaining of the paper will discuss other key parameters of the Energy Deposition Model.

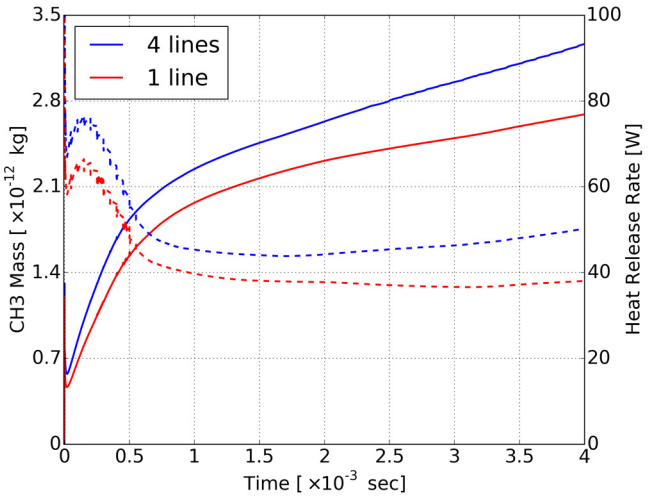

Figure 13. Overall ignition simulation behavior for thick line source and baseline setup under 2.76 bar initial pressure. Solid lines represent total CH_3 mass, and dashed lines represent total heat release rate.

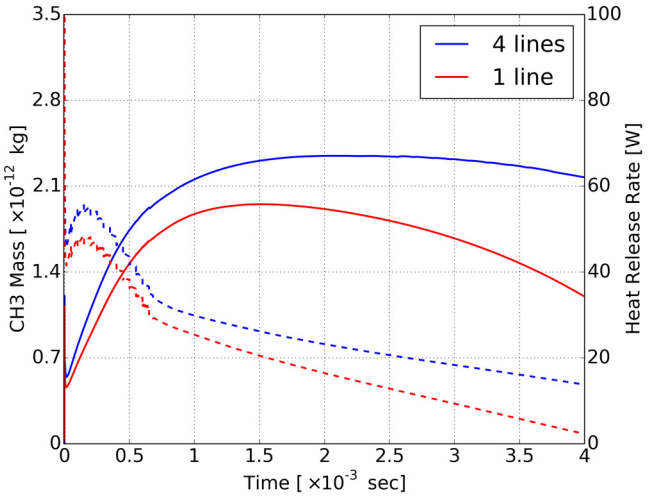

Figure 14. Overall ignition simulation behavior for thick line source and baseline setup under 1.38 bar initial pressure. Solid lines represent total CH_3 mass, and dashed lines represent total heat release rate.

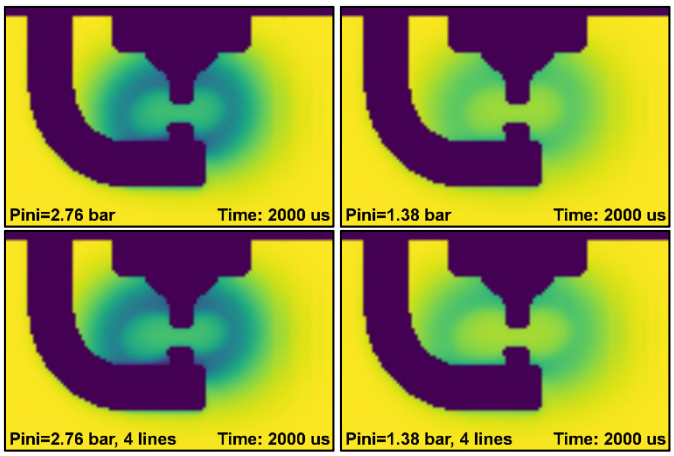

Figure 15. Comparison between numerical pseudo-schlieren realizations of thick line source and the baseline setup at 2 ms. The left column shows the cases under 2.76 bar initial pressure while the right column for 1.38 bar.

Effect of Energy Source Geometry

As is stated above, the baseline setup adopts a line shape energy source geometry realized by one column of simulation cells across the spark plug gap. Such geometry is defined to mimic the plasma channel formed during electric discharge. Meanwhile, a spherical energy source geometry is also widely used for the Energy Deposition Models [13–15]. Comparison of numerical simulations are performed between the line-shaped energy source and spherical geometries of diameters ranging from 125 μm to 1 mm. The diameter values are determined to be multiples of the minimum cell size (62.5 μm). The comparison is carried out under the same mesh setup and exactly same energy source profiles.

The first set of geometry effect results is displayed in Figure 16. With the realistic energy input, the spherical ignition sources fails to predict the ignition success under 2.76 bar initial pressure regardless of the source size. Increases in total CH_3 yields and heat release rate are observed as the source diameter increases from 125 μm to 250 μm. Such trend is similar to the cases with line-shaped sources. The increased surface area of the source is playing a dominant role given that the volumetric energy density is sufficient. However, further increasing the source's diameter does not seem to benefit the ignition. The case with 500 μm source diameter behaves similar with 250 μm case, and the 1 mm case shows the minimum CH_3 yield and heat release. The most probable cause for this reversed trend is the greatly decreased volumetric energy density at larger diameters.

The geometry effect is discussed in detail by comparing the line source with the spherical energy source of 250 μm diameter, as they share similar levels of volume and surface area. The overall ignition behavior comparison is shown in Figure 17. At a closer view into the spark plug gap at the beginning of the discharge, more differences in energy distribution between the two geometries can be observed. The volume-rendered temperature distributions across the spark plug gap at 0.2 μs are presented in Figure 18. While a relatively uniform high temperature column of the same size as the line source can be recognized for the baseline case, the spherical source cases have shown variations within the source geometry. The non-uniform temperature distribution of the spherical source is caused by the energy source term assignment. The computational cells located at the surface of the spherical source are not fully enclosed in the source boundary, thus the cell-specific energy level is essentially reduced.

As a result, the temperature gradient at the sphere boundary gets much gentler than that of the line source case. A spontaneous kernel expansion cannot be maintained without needed temperature gradient.

Another reason that the spherical energy source term may not be a favorable setup is the flame kernel shape it induces. Snapshots of pseudo-schlieren flame kernels are shown in Figure 19 for the 250 μm case. The generated flame kernel differs from the optical observation in overestimating the vertical expansion and underestimating the horizontal in its early development, and totally fades away in later time steps. In summary, the line-shaped energy source geometry is closer in nature with the electrical discharge and superior to the spherical geometry in energy distribution and flame kernel shape prediction.

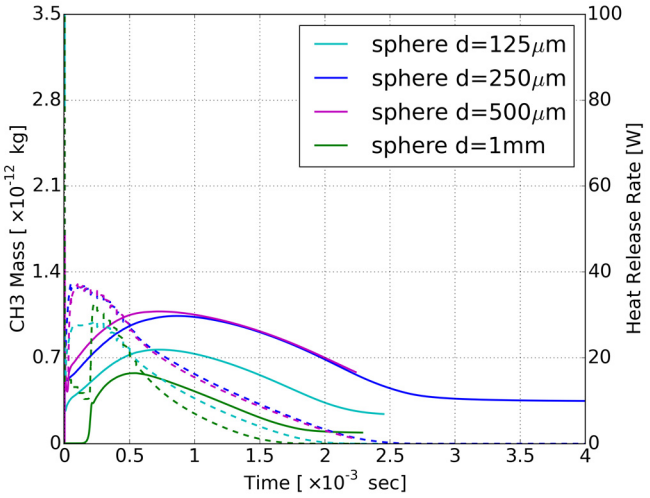

Figure 16. Overall ignition simulation behavior for spherical energy sources of different diameters under 2.76 bar initial pressure. Solid lines represent total CH_3 mass, and dashed lines represent total heat release rate.

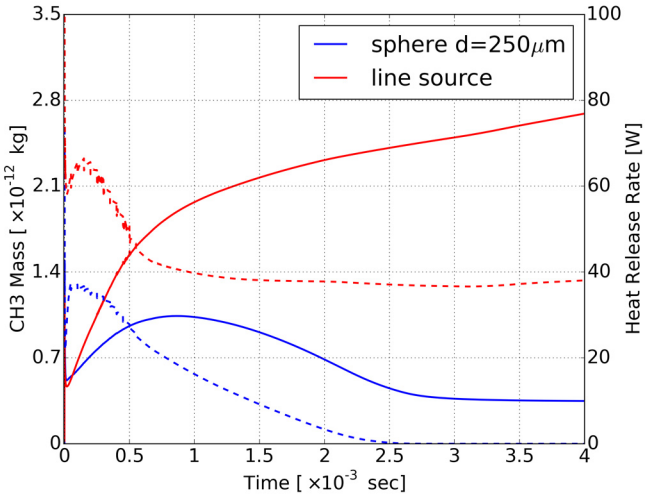

Figure 17. Overall ignition simulation behavior for spherical and line source geometry setups under 2.76 bar initial pressure. Solid lines represent total CH_3 mass, and dashed lines represent total heat release rate.

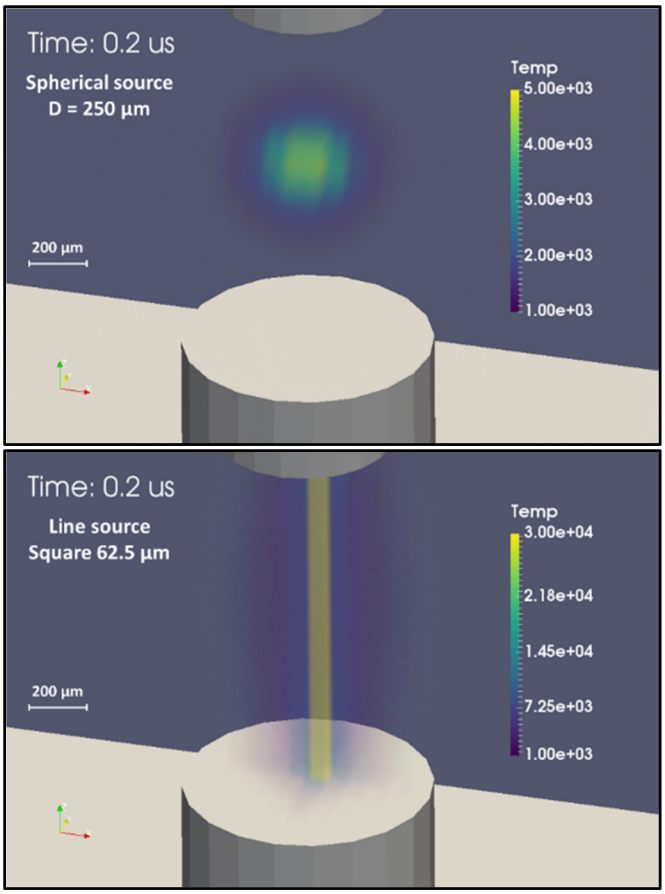

Figure 18. Temperature distribution in the vicinity of the ignition source at beginning of the discharge. The three snapshots from top to bottom show respectively the results from the spherical source of 125 µm diameter, the spherical source of 250 µm diameter, and the line source. Different color map scales are used for better representation of the distribution with different geometry setups.

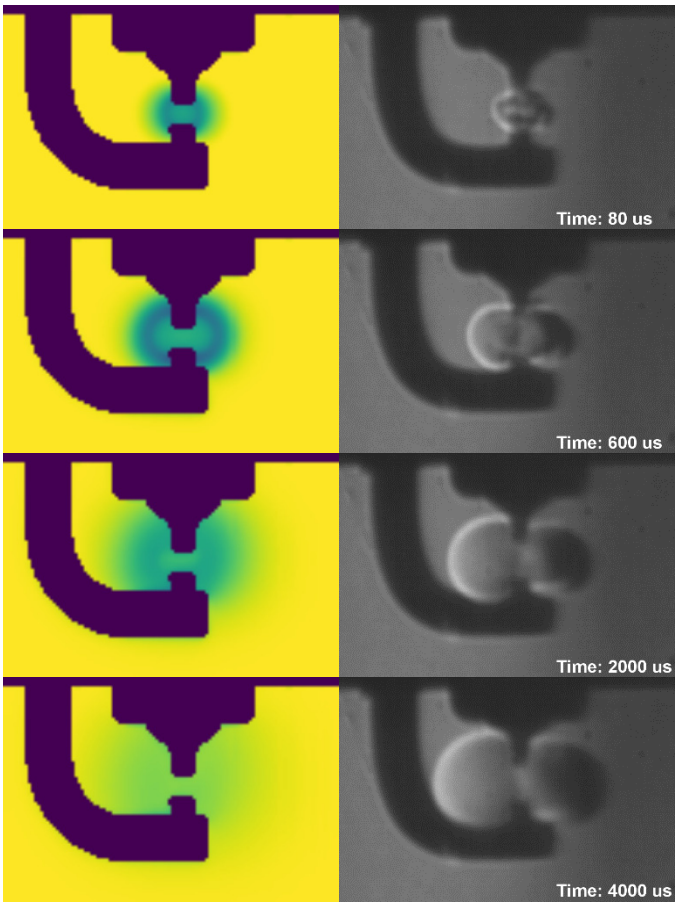

Figure 19. Comparison between numerical pseudo-schlieren realizations and optical schlieren images. The showing case is corresponding to 2.76 bar initial pressure with spherical energy source of 250 µm diameter.

Effect of Heat Transfer to Electrodes

Conjugate heat transfer (CHT) is enabled for the baseline case. In order to understand the importance to include the heat loss from flame kernels to the electrodes, two cases with extreme boundary conditions are set up for comparison. Heat loss is eliminated by setting the electrode walls adiabatic, while maximized heat transfer could be incurred by allowing as much heat as needed to pass through the electrode walls to maintain their temperature constant. Other inputs to the Energy Deposition Model are kept identical and the overall ignition behavior under 2.76 bar is shown in Figure 20. Figure 21 reports the instantaneous heat transfer behavior of the three electrode wall boundary conditions in terms of cumulative heat transfer and rate of heat transfer through the boundaries. Note that the adiabatic wall case (red lines) shows zero heat transfer. Time series of kernel expansion are represented by the pseudo-schlieren technique for the three boundary settings versus the optical data in Figure 22. The electrode colors are different for the non-CHT cases since no solid body was defined.

The constant wall temperature case has clearly introduced too much heat loss to the electrodes and quickly leads to quenching of the flame kernel. As shown in Figure 21, the constant temperature walls result in a faster heat loss rate than the CHT case during the discharge. After the discharge ends, heat transfer rate of CHT case steadily increases due to the continuation of the exothermic reactions, while that of the constant temperature wall case decreases due to the temperature drop of the quenching kernel. The kernel quenching can also be readily observed in the snapshot of 2 ms in Figure 22. The effect of the CHT model can be seen in Figure 11, which has shown the surface temperature of the electrodes in color. The energy deposition contributes to the electrode temperature increase. In the snapshot at 80 µs in Figure 11, the tips of both electrodes are heated to temperature higher than 1,000K, which helps to reduce the heat loss from the expanding kernel due to reduced temperature gradient. In addition, the CHT model managed to maintain the dynamic balance between flame kernel and electrodes temperature so that the heat conduction in the metal electrodes can be readily recognized in later time snapshots.

The adiabatic wall boundary case has shown the successful expansion of the flame kernel and the total heat release rate (Figure 20) stops decreasing at a much earlier time step than that of the baseline case. In addition, the increase rate of CH_3 mass and heat release rate is also higher for the adiabatic case than the CHT due to eliminated heat loss. However, being an unrealistic boundary condition, the adiabatic walls significantly alter the shape of the flame kernel, which is quite obvious in the 2 ms snapshot in Figure 22. The resulting flame kernel tends to expand vertically along the surfaces of the adiabatic electrodes, and the horizontal kernel expansion is greatly under predicted.

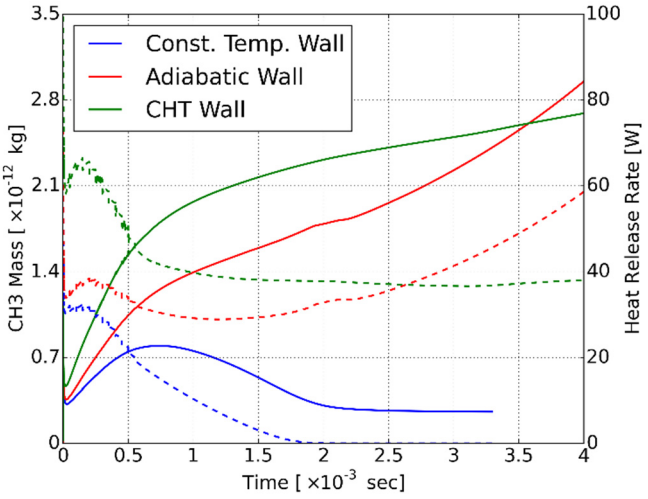

Figure 20. Overall ignition simulation behavior for three electrode wall boundary conditions under 2.76 bar initial pressure. Solid lines represent total CH_3 mass, and dashed lines represent total heat release rate.

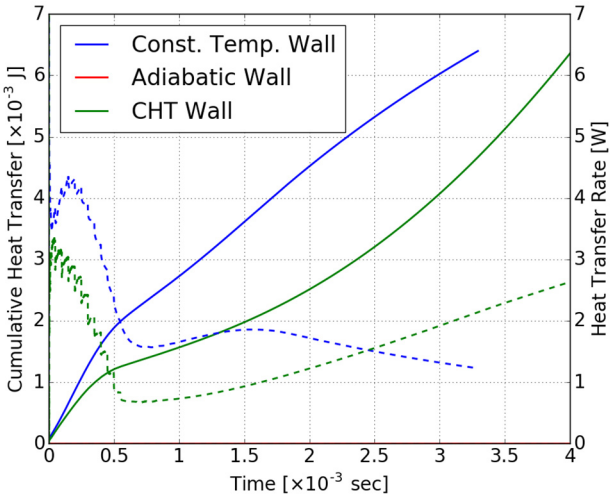

Figure 21. Instantaneous heat transfer behavior for three electrode wall boundary conditions under 2.76 bar initial pressure. Solid lines represent cumulative heat transfer, and dashed lines represent rate of heat transfer through the boundaries.

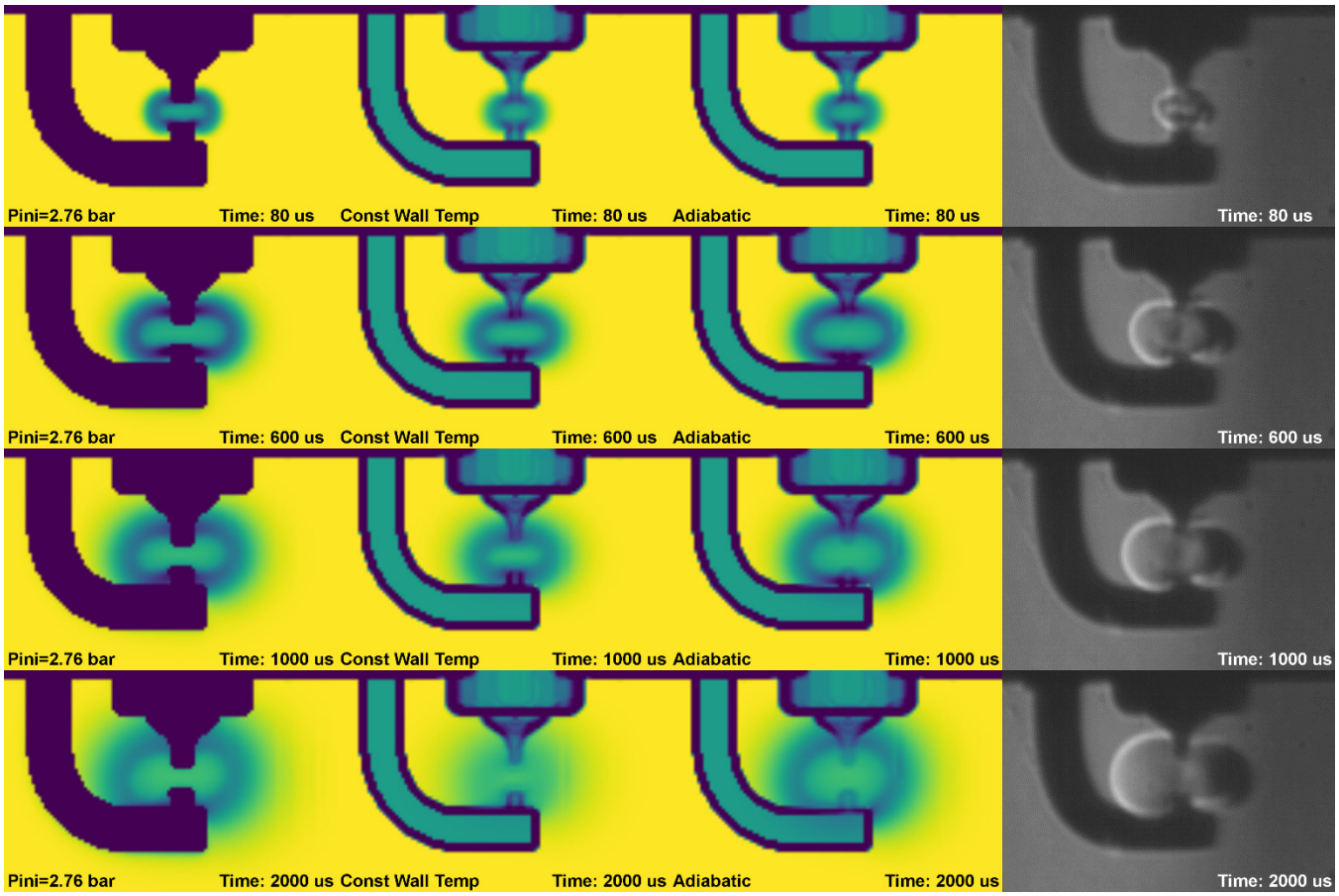

Figure 22. Comparison between numerical pseudo-schlieren realizations and optical schlieren images. The four columns of time series images represent the baseline case with CHT, the constant wall temperature boundary, the adiabatic wall boundary, and experimental data respectively from left to right.

Nonetheless, it is also worth notifying that the 80 μs snapshots for non-CHT cases actually showed better resemblance with the experiments compared to the CHT case, which leads to the curiosity to understand in more detail the initial heat transfer mode during ignition. Considering such investigation may require experimental data with finer temporal resolution, the authors tend to leave it future work as well.

The comparison study on boundary conditions have revealed another complex nature of spark ignition process: the temperature of electrode walls near the flame kernel varies rapidly during the ignition event, and it is essential to take such variation into consideration to more properly predict the kernel behavior.

Concluding Remarks

The methodology to pursue a detailed Energy Deposition Model with realistic inputs for spark ignition modeling has been performed in this paper. With properly assigned energy profile and geometry of the energy source term, the flame kernel behavior, including the general behavior of success/failure and the detailed feature of shape and expansion dynamics, can be well predicted by a simple Energy Deposition Model.

The spark plug electrode could experience rapid temperature variation during the ignition process. Unrealistic wall temperature boundary conditions usually lead to misinterpretation of the ignition phenomena. The conjugate heat transfer modeling has shown the capability to establish reasonable electrode temperature distributions for better prediction of the flame kernel behavior.

It is essential for numerical simulation validation to conduct proper comparison between simulation results and experimental data. As for schlieren images, a pseudo-schlieren procedure is proposed to generate comparable CFD realizations with optical results.

Besides further investigation on assumptions regarding variable channel size and initial heat transfer mode, the future work of this study definitely includes application of this detailed Energy Deposition Model to engine-like conditions. Efforts would be focused on properly addressing the uncertainties of the discharge characteristics under the influence of turbulent flow.

References

1. Alger, T., Gingrich, J., Mangold, B., and Roberts, C., "A Continuous Discharge Ignition System for EGR Limit Extension in SI Engines," *SAE Int J Engines* 4(1):677–692, 2011, doi:10.4271/2011-01-0661

2. Czekala, M., Johnston, B., Morganti, C., and McRoy, G., "Matching Ignition System Multi-Spark Calibration to the Burn-Rate of an Engine to Extend Ignitability Limits," SAE Technical Paper 981046, 1998, doi:10.4271/981046

3. Tanoue, K., Kuboyama, T., Moriyoshi, Y., Hotta, E., et al., "Extension of Lean and Diluted Combustion Stability Limits by Using Repetitive Pulse Discharges," SAE Technical Paper 2010-01-0173, 2010, doi:10.4271/2010-01-0173

4. Zhang, A., Cung, K., Lee, S.-Y., Naber, J., et al., "The Impact of Spark Discharge Pattern on Flame Initiation in a Turbulent Lean and Dilute Mixture in a Pressurized Combustion Vessel," *SAE Int J Engines* 6(1):435–446, 2013, doi:10.4271/2013-01-1627

5. Wallner, T., Matthias, N., Sevik, J., and Scarcelli, R., "Extending the Lean and EGR Dilute Operating Limits of a Light-Duty GDI Engine using Alternative Spark-Based Ignition," Proceedings of 2nd International Conference on Ignition Systems for Gasoline Engines (IAV), 2014

6. Law, C.K., Combustion Physics, Cambridge University Press, Cambridge, 2006

7. Smith, J., Szekely Jr, G., Solomon, A., and Parrish, S., "A Comparison of Spray-Guided Stratified-Charge Combustion Performance with Outwardly-Opening Piezo and Multi-Hole Solenoid Injectors," *SAE Int. J. Engines* 4(1):1481–1497, 2011, doi:10.4271/2011-01-1217

8. Maly, R., "Ignition model for spark discharges and the early phase of flame front growth," *Symp. Int. Combust.* 18(1):1747–1754, 1981, doi:10.1016/S0082-0784(81)80179-8

9. Tan, Z. and Reitz, R.D., "An ignition and combustion model based on the level-set method for spark ignition engine multidimensional modeling," *Combust. Flame* 145(1–2):1–15, 2006, doi:10.1016/j.combustflame.2005.12.007

10. Duclos, J.M. and Colin, O., "Arc and Kernel Tracking Ignition Model for 3D Spark-Ignition engine calculations," *Int. Symp. Diagn. Model. Combust. Intern. Combust. Engines* (1):46, 2001

11. Dahms, R.N., Drake, M.C., Fansler, T.D., Kuo, T.W., et al., "Understanding ignition processes in spray-guided gasoline engines using high-speed imaging and the extended spark-ignition model SparkCIMM. Part A: Spark channel processes and the turbulent flame front propagation," *Combust. Flame* 158(11):2229–2244, 2011, doi:10.1016/j.combustflame.2011.03.012

12. Lucchini, T., Cornolti, L., Montenegro, G., D'Errico, G., et al., "A Comprehensive Model to Predict the Initial Stage of Combustion in SI Engines," SAE Technical Paper 2013-01-1087, 2013, doi:10.4271/2013-01-1087

13. Yang, X., Solomon, A., and Kuo, T.-W., "Ignition and Combustion Simulations of Spray-Guided SIDI Engine using Arrhenius Combustion with Spark-Energy Deposition Model," SAE Technical Paper 2012-01-0147, 2012, doi:10.4271/2012-01-0147

14. Scarcelli, R., Matthias, N., and Wallner, T., "Numerical Investigation of Combustion in a Lean Burn Gasoline Engine," 2013, doi:10.4271/2013-24-0029

15. Givler, S.D., Raju, M., Pomraning, E., Senecal, P.K., et al., "Gasoline Combustion Modeling of Direct and Port-Fuel Injected Engines using a Reduced Chemical Mechanism," SAE Technical Paper 2013-01-1098, 2013, doi:10.4271/2013-01-1098

16. Ko, Y., Anderson, R.W., and Arpaci, V.S., "Spark ignition of propane-air mixtures near the minimum ignition energy: Part I.

An experimental study," *Combust. Flame* 83(1–2):75–87, 1991, doi:10.1016/0010-2180(91)90204-O

17. Richards, K.J., Senecal, P.K., and Pomraning, E., CONVERGE (Version 2.1.0), Convergent Science, Inc., Middleton, WI, 2013

18. Smith, G.P., Golden, D.M., Frenklach, M., Moriarty, N.W., et al., "GRI-MECH 3.0," http://www.me.berkeley.edu/gri_mech/

19. Maly, R.R. and Herweg, R., "Spark Ignition and Combustion in Four-Stroke Gasoline Engines," *Flow and Combustion in Reciprocating Engines*, Springer Berlin Heidelberg: 1–66, 2009

20. Paschen, F., "Ueber die zum Funkenübergang in Luft, Wasserstoff und Kohlensäure bei verschiedenen Drucken erforderliche Potentialdifferenz," *Ann. Phys.* 273(5):69–96, 1889, doi:10.1002/andp.18892730505

21. Roth, W., Guest, P.G., Elbe, G. von, and Lewis, B., "Heat Generation by Electric Sparks and Rate of Heat Loss to the Spark Electrodes," *J. Chem. Phys.* 19(12):1530–1535, 1951, doi:10.1063/1.1748116

22. Abidin, Z. and Chadwell, C., "Parametric Study and Secondary Circuit Model Calibration Using Spark Calorimeter Testing," SAE Technical Paper 2015-01-0778, 2015, doi:10.4271/2015-01-0778

23. Sher, E., Ben-Ya'Ish, J., and Kravchik, T., "On the birth of spark channels," *Combust. Flame* 89(2):186–194, 1992, doi:10.1016/0010-2180(92)90027-M

24. Ishii, K., Tsukamoto, T., Ujiie, Y., and Kono, M., "Analysis of ignition mechanism of combustible mixtures by composite sparks," *Combust. Flame* 91(2):153–164, 1992, doi:10.1016/0010-2180(92)90097-9

25. Jozef, J., Michikata, K., and Mitsuhiro, T., "Flammability Limits," *Combustion Phenomena*, CRC Press, 2009

26. Brownlee, C., Pegoraro, V., Shankar, S., McCormick, P., et al., "Physically-based interactive schlieren flow visualization," 2010, doi:10.1109/PACIFICVIS.2010.5429599

Acknowledgments

The submitted manuscript has been created by UChicago Argonne, LLC, Operator of Argonne National Laboratory ("Argonne"). Argonne, a U.S. Department of Energy Office of Science laboratory, is operated under Contract No. DE-AC02-06CH11357. The U.S. Government retains for itself, and others acting on its behalf, a paid-up nonexclusive, irrevocable worldwide license in said article to reproduce, prepare derivative works, distribute copies to the public, and perform publicly and display publicly, by or on behalf of the Government.

This research is funded by DOE's Vehicle Technologies Program, Office of Energy Efficiency and Renewable Energy. The authors would like to express their gratitude to Gurpreet Singh and Leo Breton, program managers at DOE, for their support.

The experimental data were obtained at Michigan Technological University in collaboration with Ford Motor Company under Department of Energy Award Number DE-EE0003332. The authors would like to thank Garlan Huberts, Michael Czekala, and Qiuping Qu for their informative discussions.

Numerical simulations were run on the Blues Cluster at the LCRC, Argonne National Laboratory. Special thanks to Ray Bair and John Blaas for their help in facilitating the simulation work.

Contact Information

Anqi Zhang, PhD

Argonne National Laboratory, Energy System Division, Center for Transportation Research, 9700 S. Cass Ave, Argonne, IL 60439, Phone: 630-252-2147, Email: anqiz@anl.gov

Definitions/Abbreviations

DPIK	Discrete Particle Ignition Kernel
AKTIM	Arc and Kernel Tracking Ignition Model
SparkCIMM	Spark Channel Ignition Monitoring Model
CHT	Conjugate Heat Transfer
RNG	Renormalization Group
RANS	Reynolds-averaged Navier–Stokes